



Construction and multifunctional of hypercrosslinked porous organic polymers containing ferrocene unit for high-performance iodine adsorption and supercapacitor

Mohamed Gamal Mohamed^{a,b,1,*}, Ahmed M. Elewa^{c,1}, Meng-Syuan Li^a, Shiao-Wei Kuo^{a,d,*}

^a Department of Materials and Optoelectronic Science, Center of Crystal Research, National Sun Yat-Sen University, Kaohsiung 80424, Taiwan

^b Chemistry Department, Faculty of Science, Assiut University, Assiut 71516, Egypt

^c Department of Chemical Engineering, National Tsing Hua University, Hsinchu 300044, Taiwan

^d Department of Medicinal and Applied Chemistry, Kaohsiung Medical University, Kaohsiung 807, Taiwan

ARTICLE INFO

Keywords:

Hypercrosslinked porous organic polymers
Friedel-Crafts reaction
Ferrocene
I₂ uptake
Supercapacitors

ABSTRACT

Background: The efficient capture of iodine and the reduction of CO₂ emissions has become increasingly important in recent years due to their potential threats to human health and the environment. Hypercrosslinked Porous Organic Polymers (HPPs) are considered excellent adsorbent materials for these purposes due to their high surface areas, controllable structures, and thermal/chemical stabilities.

Methods: This work aimed to produce Fe-Bi HPP and An-Bi HPP materials for use in I₂ uptake and supercapacitors applications. The preparation of these materials involved utilizing the Friedel-Crafts reaction of Fe-Di imidazole and An-Di imidazole with 4,4'-bis(chloromethyl)-1,1'-biphenyl (Bi-2Cl) in the presence of anhydrous FeCl₃.

Significant findings: These materials exhibited a narrow range of pore sizes in the micropore range and had a high specific surface area of approximately 850 m² g⁻¹. According to the results of the electrochemical analysis, the Fe-Bi HPP demonstrated an energy density of 21 Wh Kg⁻¹ and capacitance of 147 F/g. The adsorption experiments demonstrated the effectiveness of both materials in capturing iodine. The Fe-Bi HPP has superior efficiency compared to the An-Bi HPP, which can be attributed to its larger surface area and the presence of the ferrocene unit. It exhibits an impressive I₂ adsorption uptake of 112.84 mg g⁻¹.

1. Introduction

The excessive burning of petroleum products has resulted in contamination of the environment, increased CO₂ emissions, and the discharge of hazardous particles from vehicle exhaust [1–10]. Scientists have focused on discovering new and effective alternatives for storing renewable energy to address this issue [10–15]. Electrochemical energy storage has emerged as one of the most practical approaches to addressing energy shortages [15–20]. Several electrochemistry-based devices are developed, ranging from batteries to conventional capacitors and supercapacitors (SCs) [21–25]. These devices possess desirable features such as safety, suitable capacity intensity, fast charge/discharge rates, and high cycle reliability [21–30]. Among these devices, SCs are the most advanced and promising type for this application, with

additional benefits including low cost, exceptional longevity, and high-rate efficiency [31–35]. Supercapacitors (SCs) store energy through two different mechanisms, non-faradaic and faradaic. In the non-faradaic mechanism, ionic charges are generated electrostatically between the electrodes and electrolytes, whereas in the faradaic mechanism, reversible redox reactions occur on a solid surface [35–40]. Consequently, the electrode material is one of the primary criteria that influence the effectiveness of SCs. Electrode materials for SCs have been widely explored using a variety of organic and inorganic materials. [41–45]. Despite their numerous advantages, inorganic materials feature a few disadvantages that create environmental concerns [41–45], such as depletion of resources and pollution. Since organo-electrodes have greater qualities, such as excellent efficiency, low energy consumption, and environmental friendliness, there has

* Corresponding authors at: Department of Materials and Optoelectronic Science, Center of Crystal Research, National Sun Yat-Sen University, Kaohsiung 80424, Taiwan.

E-mail addresses: mgamal.eldin12@yahoo.com (M.G. Mohamed), kuosw@faculty.nsysu.edu.tw (S.-W. Kuo).

¹ These two authors contributed equally to this work.

<https://doi.org/10.1016/j.jtice.2023.105045>

Received 8 May 2023; Received in revised form 26 June 2023; Accepted 12 July 2023

Available online 27 July 2023

1876-1070/© 2023 Taiwan Institute of Chemical Engineers. Published by Elsevier B.V. All rights reserved.

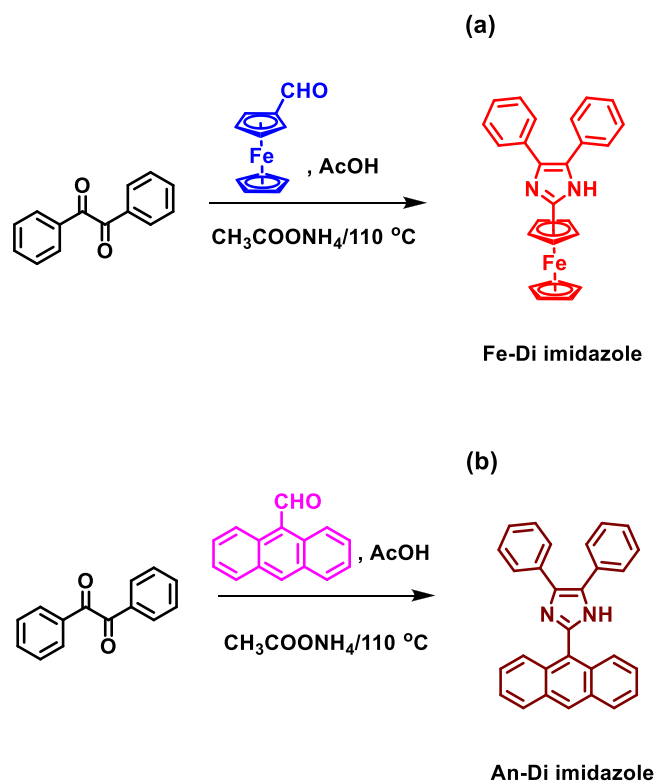


Fig. 1. Schematic synthesis route for (a) Fe-Di imidazole and (b) An-Di imidazole.

been an increase in interest in using them [41–45]. POPs are a kind of porous material that has become popular in a number of applications, including the removal of pollutants, sensing, the storage and separation of CO₂, battery technology, and medication delivery [45–53]. Among

the different types of POPs, Hypercrosslinked Porous Organic Polymers (HPPs) have gained significant attention in the field of supercapacitors due to their unique properties, including structural flexibility, variability in pore structures, and high physicochemical stability [54–55]. HPPs possess large pore structures, making them ideal as organic electrode materials for supercapacitors [55–59]. Additionally, the specific conjugated structure of HPPs, which features redox activity, results in excellent electrochemical properties [55–59]. Currently, the most efficient method for incorporating strong binding sites into amorphous materials is by introducing moieties with a high affinity into the framework. Lewis acidic iodine molecules are known to specifically bind with nitrogen (N) and sulfur (S) atoms, as well as molecular building blocks that are rich in π -bonds. However, there is a strong desire to develop access to molecular building blocks with even higher electron density than those found in typical π -bond-rich groups such as triple bonds and phenyl rings. Such building units would create a framework with a stronger binding capacity for I₂. Ferrocene (Fe) is a building block that is highly sought after due to its high electron density and its effectiveness as an electron donor has been demonstrated in previous studies [60,61]. The stable sandwich structure and redox capability of ferrocene have generated significant interest in the field of organometallic chemistry [60–64]. Incorporating the ferrocene moiety into polymer structures is known to impart unique properties, including exceptional magnetic, catalytic, electrical, sensing, and optical characteristics [60–65]. This has made ferrocene an attractive building block for designing novel polymers. Polymer materials based on ferrocene exhibit potential for a wide range of applications, including memory devices, redox batteries, catalysis, and energy storage [65–67]. These exceptional properties make ferrocene a promising and novel option for capturing iodine.

Iodine (I₂) serves as a typical radioactive pollutant. It presents a significant worry for the atmosphere, surface water, and subsurface water, whether in solid or fluid states. The gaseous form of iodine is particularly concerning due to its rapid dispersion. Iodine can manifest in the environment in different chemical forms: organic (CH₃I),

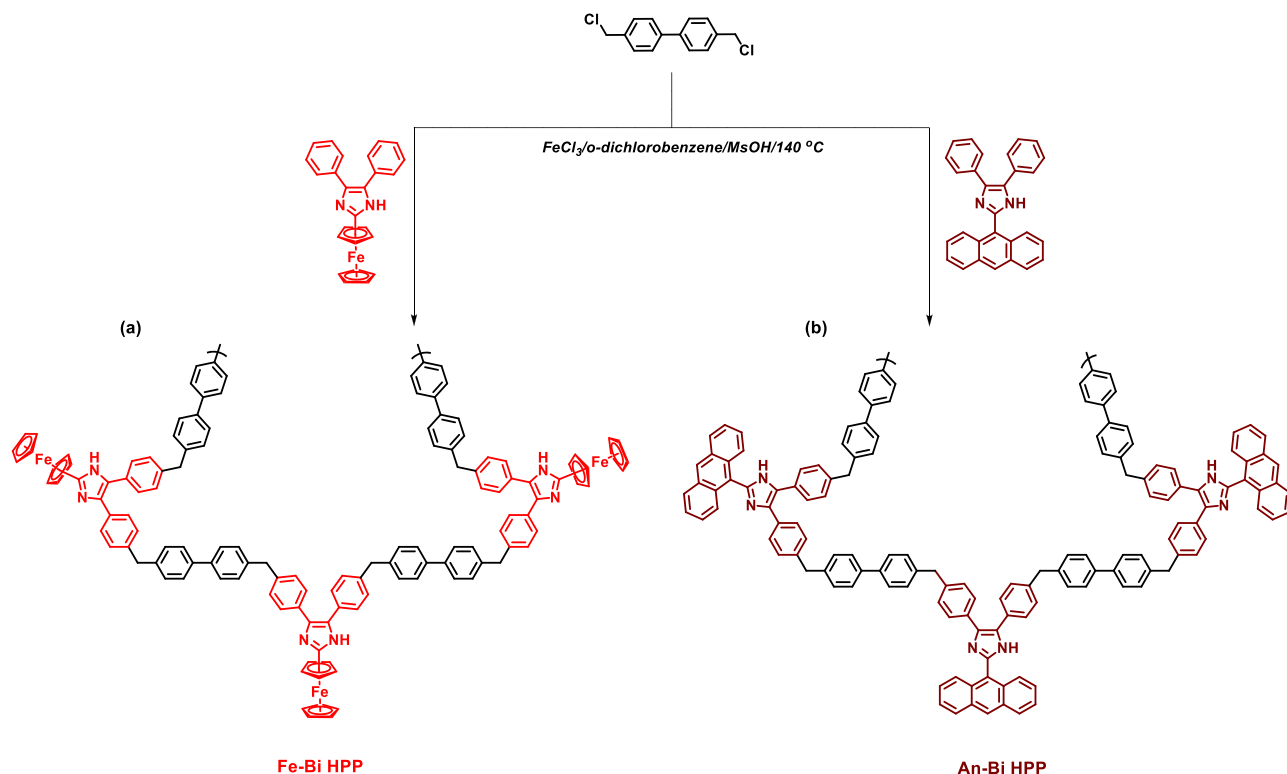


Fig. 2. Schematic synthesis route for (a) Fe-Bi HPP and (b) An-Bi HPP.

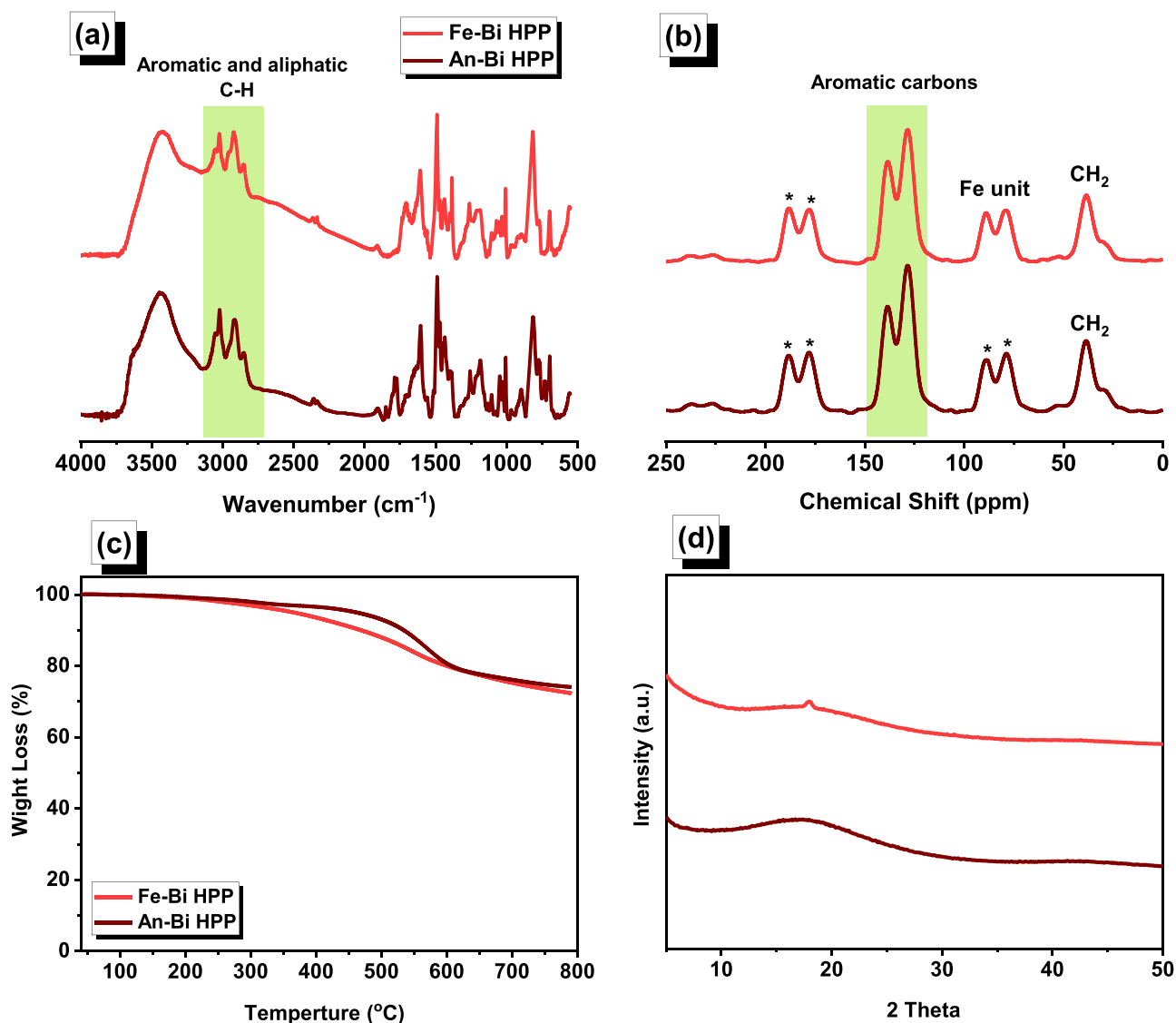


Fig. 3. FTIR spectra (a), ¹³C NMR spectra (b), TGA curves (c), and XRD patterns of the Fe-Bi and An-Bi HPPs samples.

Table 1
Summarized TGA, BET, and capacitance data of Fe-Bi HPP and An-Bi HPP.

Sample	T _{d5} (°C)	T _{d10} (°C)	Char Yield (wt. %)	Surface Area (m ² /g)	Pore Volume (cm ³ /g)	Pore Size (nm)	Capacity at 0.5 A g ⁻¹ (F g ⁻¹)
Fe-Bi HPP	365	469	72	898	0.99	1.40	147
An-Bi HPP	462	534	74	844	0.79	1.07	106

inorganic (I^- , IO_4^- , and IO_3^-), and elemental iodine (I_2). This variability is primarily attributed to its volatility and mobility. The radioactivity of ¹²⁹I poses a grave hazard to both human life and the environment, owing to its extended half-life (1.57×10^7 years). Consequently, it accumulates and endures in the environment while easily mingling with surface water. Concerning ¹³¹I, two primary issues arise: (i) the accidental emission of radiation, which can harm living organisms due to its high activity and half-life of 8.04 days, and (ii) its potential incorporation into the respiratory and food processing systems of humans. To address these radioactive iodine isotopes and associated problems, it is imperative to develop suitable adsorbents and uptake mechanisms. The development

of a convenient method for the effective management of nuclear waste aims to achieve controlled release and recycling of iodine while considering environmental concerns. Two prevalent methods for capturing iodine are solid and wet processes. In the wet process, a solvent undergoes a reaction with iodine species and removes them as a compound from either the gas or liquid phase. On the other hand, the solid adsorption process involves the use of solid materials that possess the ability to attract vapor or aqueous iodine to their surface upon contact. Previous studies focused on adsorbing I_2 in a closed system, utilizing saturated I_2 vapor at 75 °C, and measuring the subsequent increase in mass under room temperature conditions to determine adsorption capacity. However, radioactive iodine (¹²⁹I and ¹³¹I) originating from nuclear waste has a propensity to enter water bodies due to its volatility. While many porous materials are extensively used for capturing iodine vapor, there is limited research on the uptake of iodine from water. Therefore, it is crucial to remove iodine molecules from aqueous solutions, where iodine typically exists in the form of I_3^- . The diameter of I_3^- is 5.3 Å [68], making it easily loadable into porous materials. To address this, we conducted iodine adsorption experiments in aqueous solutions using UV-vis absorption spectra.

In this study, we prepared two new HPPs materials, namely Fe-Bi and An-Bi HPPs, through the reaction of Bi-2Cl with Fe-Di imidazole and An-

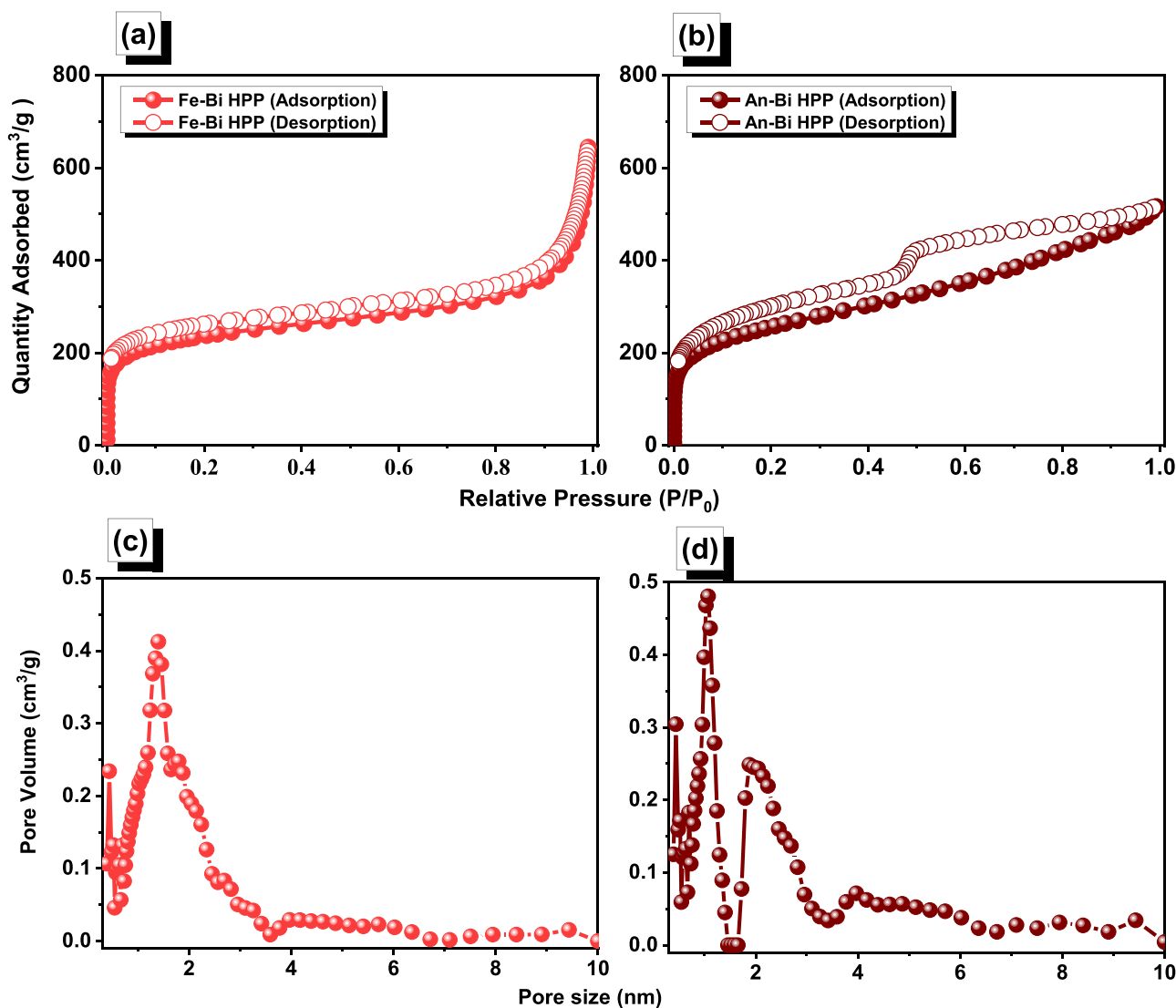


Fig. 4. N_2 sorption (a, b) and pore size distribution (c, d) profiles of Fe-Bi HPP (a, c), and An-Bi HPP (b, d), were recorded at 77 K.

Di imidazole in 1,2-dichlorobenzene and methanesulfonic acid, in the presence of $FeCl_3$. We carefully examined and discussed the molecular structures, porosity, morphology, thermal stability, and crystallinity of these materials using FTIR, ssNMR, SEM, TEM, BET, XRD, and TGA measurements. The BET analysis revealed that both Bi-HPPs showed surface areas of up to $850\text{ m}^2\text{ g}^{-1}$, featuring *meso* and microporous structures. Based on our findings, we anticipate that Fe-Bi and An-Bi HPPs hold great potential as promising precursors for energy storage applications and the adsorption of I_2 .

2. Experimental

2.1. Materials

Benzil (98%), ferrocenecarboxaldehyde (Fe-CHO, 98%), 9-anthracenecarboxaldehyde (An-CHO, 97%), ammonium acetate (CH_3COONH_4 , 99.99%), 4,4'-bis(chloromethyl)-1,1'-biphenyl (Bi-2Cl, 95%) Ferric chloride ($FeCl_3$, 99.9%), methanesulfonic acid (CH_3SO_3H , 99%), acetic acid (AcOH, 99%) and 1,2-dichlorobenzene were purchased from Sigma-Aldrich. Tetrahydrofuran (THF), dichloromethane (DCM), methanol (MeOH), and acetone were purchased from Acros.

2.2. Synthesis of 2-(ferrocen-9-yl)-4,5-diphenyl-1H-imidazole (Fe-Di imidazole)

To prepare Fe-Diimidazole, we mixed 1 g of benzil (4.76 mmol), 1.23 g of Fe-CHO (5.75 mmol), 1.83 g of CH_3COONH_4 (23.74 mmol), and 10 mL of AcOH in a Schlenk tube that had been dried using a flame. The mixture was kept at $95\text{ }^\circ\text{C}$ for 24 h. Afterward, we filtered the resulting solid and washed it with different organic solvents to eliminate any residual reagents. Finally, we dried the solid at $60\text{ }^\circ\text{C}$ overnight, yielding Fe-Di imidazole in the form of a black powder (3 g, yield: 63%).

2.3. Synthesis of 2-(anthracen-9-yl)-4,5-diphenyl-1H-imidazole (An-Di imidazole)

To prepare An-Diimidazole, we introduced 1 g of benzil (4.76 mmol), 1.18 g of An-CHO (5.72 mmol), 1.83 g of CH_3COONH_4 (23.74 mmol), and 10 mL of AcOH into a Schlenk tube that had been dried over a flame. The mixture was kept at $95\text{ }^\circ\text{C}$ for 24 h. Afterward, we filtered the resulting solid and washed it with different organic solvents to eliminate any residual reagents. Finally, we dried the solid at $60\text{ }^\circ\text{C}$ overnight, yielding An-Di imidazole as a brown powder (3.3 g, yield: 69%).

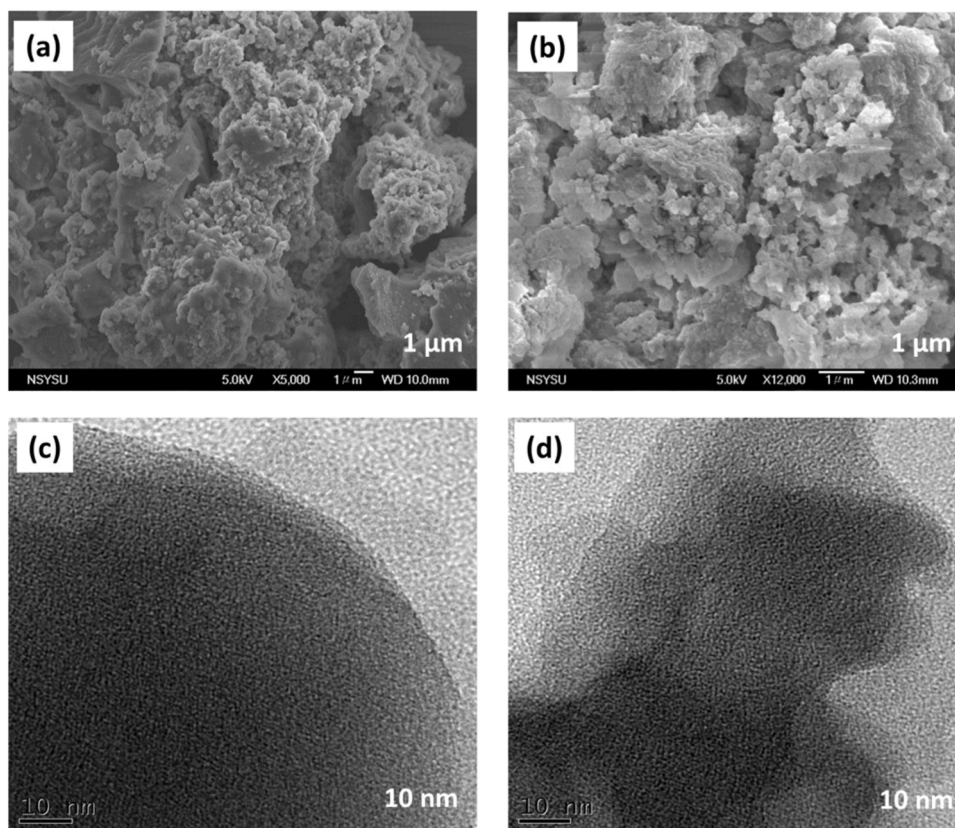


Fig. 5. SEM (a, b) and TEM (c, d) images of Fe-Bi HPP (a, c), and An-Bi HPP (b, d).

2.4. Synthesis of Fe-Bi HPP

To synthesize Fe-Bi HPP, Fe-Di imidazole (0.5 g, 1.24 mmol), Bi-2Cl (1.855 g, 7.42 mmol), FeCl_3 (1.204 g, 7.42 mmol), $\text{CH}_3\text{SO}_3\text{H}$ (1.45 mL), and 1,2-dichlorobenzene (30 mL). The mixture was refluxed at 140 °C under nitrogen flow for 2 days. After the reaction was complete, the resulting solid was washed with different organic solvents to eliminate any residual reagents. Finally, we dried the solid at 60 °C overnight, to obtain Fe-Bi HPP as a black powder with a yield of 0.24 g (yield: 48%).

2.5. Synthesis of An-Bi HPP

A mixture of An-Di imidazole (0.5 g, 1.26 mmol), Bi-2Cl (1.892 g, 7.57 mmol), FeCl_3 (1.227 g, 7.56 mmol), $\text{CH}_3\text{SO}_3\text{H}$ (1.47 mL), and 1,2-dichlorobenzene (30 mL) in a round-bottom flask at 140 °C for 2 days. After the reaction was complete, the resulting solid was washed with different organic solvents to eliminate any residual reagents. Finally, we dried the solid at 60 °C overnight, to obtain a brown powder of a brown powder of An-Bi HPP (0.3 g, yield: 60%).

2.6. Preparation of Bi-HPPs materials for I_2 iodine uptake measurements

In order to investigate the iodine capture capacities of the Bi-HPPs materials in a solution, we conducted the following procedure. First, we established a calibration plot using a solution of iodine in cyclohexane without any samples. Subsequently, we immersed 10 mg of each sample in a sealed glass bottle containing an iodine/cyclohexane solution (0.2 mg mL^{-1} , 10 mL). The solution was stirred for a period of time and then subjected to centrifugation before measuring the UV-Visible absorption spectroscopy. To assess the efficiency of iodine removal from the solution by Bi-HPPs samples, we recorded the UV-vis spectra of the iodine aqueous solutions at different time intervals, maintaining a temperature of 25 °C.

3. Results and discussion

3.1. Synthesis and characterization of Fe-Di imidazole, An-Di imidazole, Fe-Bi HPP and An-Bi HPP

The Fe-Di imidazole was synthesized by reacting Fe-CHO and benzil with $\text{CH}_3\text{COONH}_4$ in the presence of AcOH, as shown in Fig. 1(a). An-Di imidazole was obtained by reacting benzil with $\text{CH}_3\text{COONH}_4$ and An-CHO in AcOH, as shown in Fig. 1(b). The molecular structures of both Fe-Di imidazole and An-Di imidazole were confirmed using FTIR and NMR measurements, as depicted in Figs. S1–S6. The absorption peaks corresponding to C = C, C–H aromatic, and NH units were observed at 1593, 3044, and 3204 cm^{-1} , respectively for Fe-Di imidazole [Fig. S1], while for An-Di imidazole, they were centered at 1596 and

3049, and 3162 cm^{-1} , respectively [Fig. S2] [69,70]. The ^1H and ^{13}C NMR spectra of both Fe-Di imidazole and An-Di imidazole were recorded in diluted DMSO- d_6 , as shown in Figs. S3–S6. The ^1H NMR spectrum of Fe-Di imidazole featured signals at 12.18 ppm for N–H units, 7.93–7.18 ppm for the phenyl rings, and the peaks at 4.94, 4.35, and 4.14 ppm for the ferrocene unit [Fig. S3]. The ^1H NMR spectrum of An-Di imidazole featured signals at 12.94 ppm for N–H units, and 8.20–7.24 ppm for the aromatic carbons [Fig. S4]. The ^{13}C NMR spectrum of Fe-Di imidazole featured bands in the range of 137.01–126.94 ppm for the carbon nuclei of the aromatic ring, and 76.13, 69.57, and 66.66 ppm for the ferrocene unit, as shown in Fig. S5. The ^{13}C NMR pattern of An-Di imidazole featured bands in the range of 137.71–126.30 ppm for aromatic carbons, as depicted in Fig. S6. Fig. 2 outlines the step-by-step process for synthesizing Fe-Bi HPP and An-Bi HPP. In Fig. 2(a) and (b), the initial reaction involves combining Fe-Di imidazole or An-Di imidazole with anhydrous FeCl_3 and Bi-2Cl in the presence of 1,2-dichlorobenzene and $\text{CH}_3\text{SO}_3\text{H}$. This reaction produces Fe-Bi HPP, which is a black powder, and An-Bi HPP, which appears as a brown powder. The FTIR spectra of Fe-Bi HPP and An-Bi HPP were

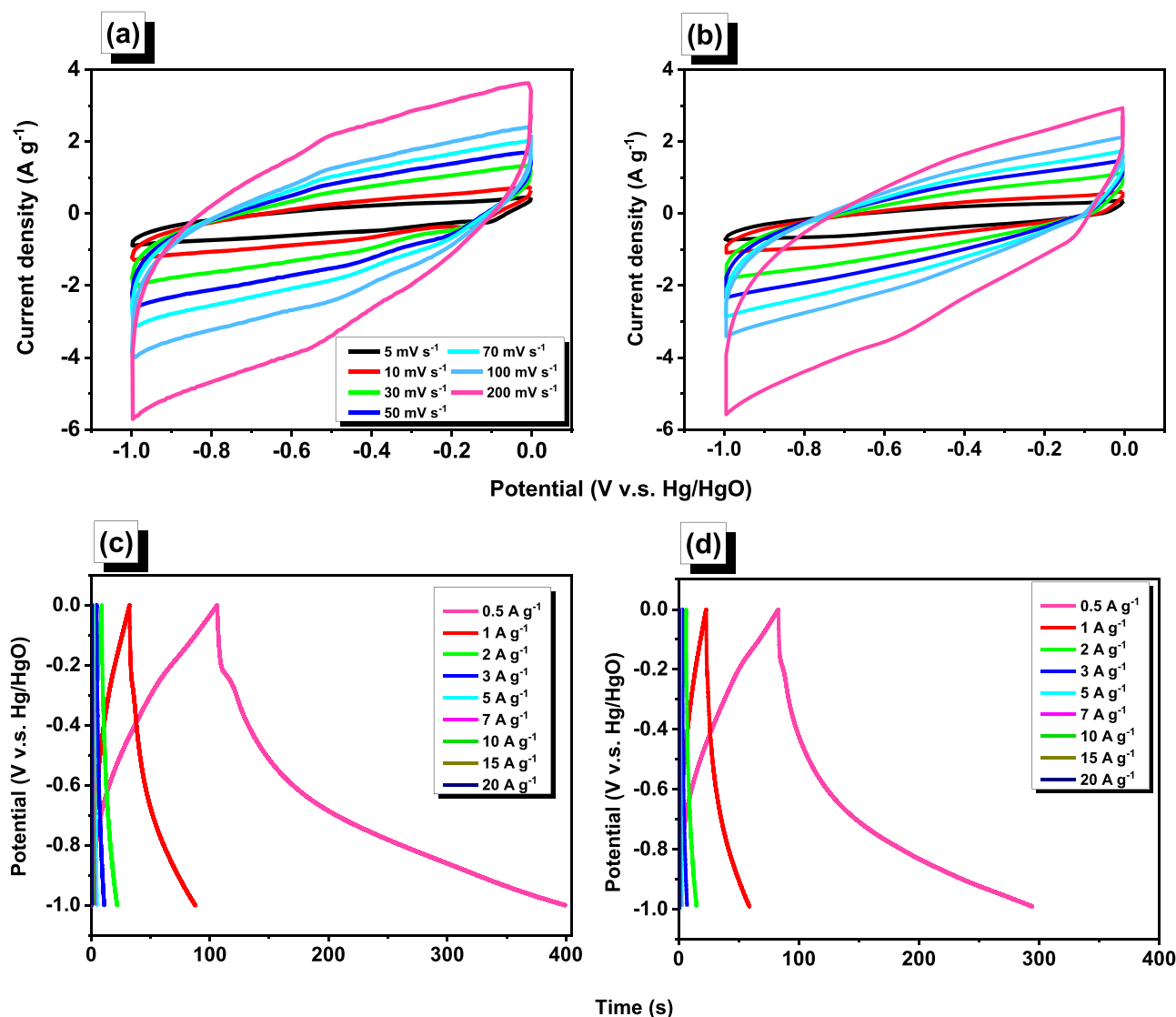


Fig. 6. CV (a, b) and GCD (c, d) profiles of Fe-Bi HPP (a, c) and An-Bi HPP (b, d).

recorded at room temperature and presented in Fig. 3(a). In the spectra of Fe-BiHCP, the C=C aromatic groups were represented by FTIR signals in the range of 1489–1608 cm^{-1} , while the C–H aliphatic groups were indicated by a signal at 2924 cm^{-1} . The FTIR signals of An-BiHPP in the range of 1486–1609 cm^{-1} due to their C=C aromatic groups, while the signal at 2918 cm^{-1} was associated with the C–H aliphatic groups. The vanishing of the C–Cl bond and the appearance of signals of C–H aliphatic groups in both Fe-Bi HPP and An-Bi HPP suggest the formation of cross-linked networks. Fig. 3(b) shows that the chemical compositions of Fe-Bi HPP and An-Bi HPP were verified using solid-state ^{13}C NMR measurement (ssNMR). The phenyl groups in Fe-Bi and An-Bi HPPs were identified by the appearance of characteristic signals at 145.06–118.25 ppm and 146.09–118.63 ppm, respectively. The peaks observed in the ssNMR spectrum of Fe-Bi HPP from 79.56 to 88.69 ppm provide strong evidence for the presence of ferrocene units in Fe-Bi HPP. This finding agrees with the data reported by Okada et al. [71] further confirming the existence of ferrocene units in Fe-Bi HPP. The weight reduction in the descending thermal curves depicted in Fig. 3(c) indicates that the Fe-Bi HPP and An-Bi HPP undergo thermal degradation. TGA measurements reveal that Fe-Bi HPP exhibits T_{d5} , T_{d10} , and char yield values of 365 $^{\circ}\text{C}$, 469 $^{\circ}\text{C}$, and 72%, respectively, while An-Bi HPP displays T_{d5} , T_{d10} , and char yield values of 462 $^{\circ}\text{C}$, 534 $^{\circ}\text{C}$, and 74%. These values, along with those for other Bi-HPPs materials, are summarized in Table 1,

demonstrating the excellent thermal stability of our porous materials. The XRD profile of both Fe-Bi HPP and An-Bi HPP in Fig. 3(d) indicates that these materials possess semicrystalline properties.

N_2 adsorption/desorption measurements were used to confirm the porosity properties of the Fe-Bi HPP and An-Bi HPP at 77 K, as shown in Fig. 4 and Table 1. Prior to the analyses, the Bi-HPPs samples underwent vacuum degassing for 12 h (at 150 $^{\circ}\text{C}$). Based on the IUPAC system, the adsorption profile indicates that the Fe-Bi HPP had IV adsorption isotherms (Fig. 4(a)), while the An-Bi HPP had type IV (Fig. 4(b)). Moreover, the Fe-Bi HPP displayed an improved N_2 uptake capacity at both low and high-pressure regions in its BET profile, which suggests that *meso* and micropores are present within the framework of Fe-Bi HPP. On the other hand, the An-Bi HPP showed a hysteresis loop due to the presence of ink-bottle-type pores. The specific surface areas of Fe-Bi HPP and An-Bi HPP were 898 and 844 $\text{m}^2 \text{g}^{-1}$, respectively. Using nonlocal density functional theory (NLDFT), the pore size distributions of Fe-Bi HPP and An-Bi HPP were estimated, yielding micropore diameters of 1.40 and 1.07 nm, respectively (Fig. 4(c) and (d)). The pore volume was 0.99 $\text{cm}^3 \text{g}^{-1}$ for Fe-Bi HPP and 0.79 $\text{cm}^3 \text{g}^{-1}$ for An-Bi HPP.

To examine the ordering and morphology characteristics of Fe-Bi HPP and An-Bi HPP, SEM, and HR-TEM techniques were used, as illustrated in Fig. 5. The SEM images demonstrate that Fe-Bi HPP is composed mainly of aggregated nanospheres in clusters, while An-Bi

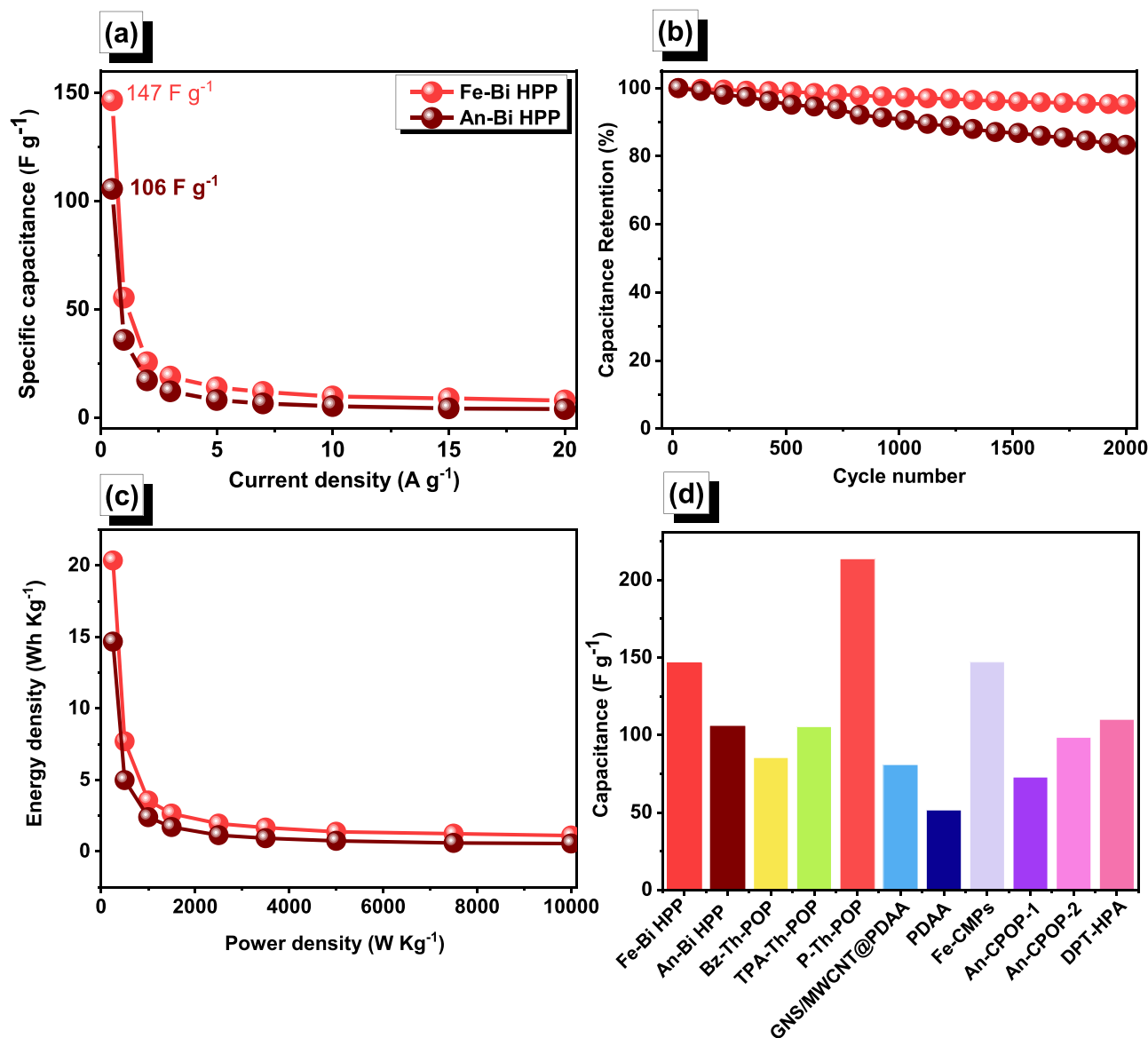


Fig. 7. Specific capacitance (a), durability (b), and Ragone (c) profiles of Fe-Bi HPP, and An-Bi HPP. (d) Comparison of electrochemical performances of two Bi-HPPs materials with other reported porous polymer materials.

HPP forms irregular rock-like clusters [Fig. 5(a) and (b)]. The findings from HR-TEM images suggest that both HPPs possess a porous structure characterized by a uniform pore diameter, but no long-range ordering was detected [Fig. 5(c) and (d)].

3.2. Supercapacitor performance of Fe-Bi HPP and An-Bi HPP materials

The unique structure of ferrocene, resembling a sandwich, and its high electron density make it capable of exhibiting remarkable redox performance, thus allowing it to function effectively as an electron donor. These characteristics combine features of both organic and metallic compounds [60,61,67]. To study the electrochemical properties of Bi-HPPs, cyclic voltammetry (CV) and galvanostatic charge-discharge (GCD) measurements were carried out in a three-electrode system comprising glassy carbon, platinum, and Hg/HgO electrodes, respectively. The measurements were performed in an aqueous solution of 1.0 M KOH. To analyze the electrochemical properties of Fe-Bi HPP and An-Bi HPP, their CV curves [shown in Fig. 6(a) and (b)] were recorded by sweeping the potential over a range of -1.0 to 0.0 V (vs Hg/HgO) at different scan rates varying from 5 to $200 mV s^{-1}$. The observed

rectangle-like humped shape of the curves is a characteristic feature of electric double-layer capacitance (EDLC), which suggests that the prepared HPPs remained stable during the current sweep. While the shape of the curves remained unchanged, the peak current density showed an increase with an increase in the CV scan rate, indicating good electron-transporting properties and facile kinetics. The GCD profiles of Fe-Bi HPP and An-Bi HPP [Fig. 6(c) and (g)] show triangular shapes, which are typical features of pseudocapacitance behavior. The Fe-Bi HPP material had a longer discharge time and bigger discharge area than the An-Bi HPP material at all current densities, indicating that Fe-Bi HPP had higher specific capacities than the An-Bi HPP.

Measurements of the specific capacitance of the Bi-HPPs electrodes were taken at different current densities. It was observed that at a current density of $0.5 A g^{-1}$, the capacitance values for Fe-Bi HPP and An-Bi HPP were found to be 147 and $106 F g^{-1}$, respectively [Fig. 7(a)]. Fe-Bi HPP exhibits better electrochemical performance than An-Bi HPP because it contains a ferrocene moiety and has a larger surface area [31, 67,72]. The cycling stability of the Bi-HPPs electrodes was evaluated at $10 A g^{-1}$, and after 2000 cycles of charge and discharge, the retention values were found to be 95.24% and 83.33% for Fe-Bi HPP and An-Bi

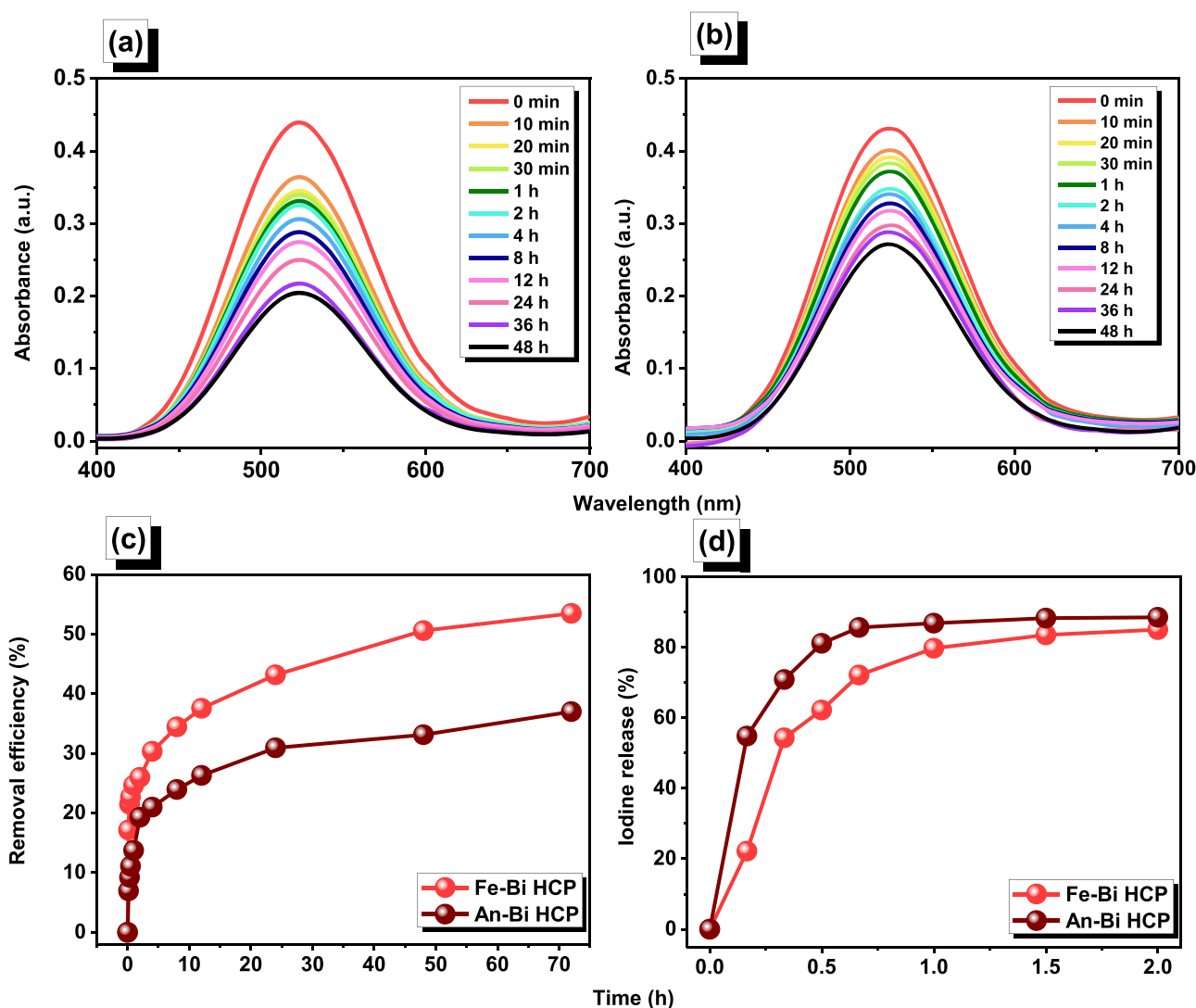


Fig. 8. UV-vis spectra at different times for Fe-Bi HPP (a), and An-Bi HPP (b) in an iodine/cyclohexane solution (200 mg L^{-1} , 10 mL). Kinetic studies of Fe-Bi HPP and An-Bi HPP (c) in iodine/cyclohexane solutions (200 mg L^{-1} , 10 mL). Release process (d) of Fe-Bi HPP and An-Bi HPP by heating at 130°C .

HPP, respectively [Fig. 7(b)]. These results suggested that Bi-HPPs materials had good cycling stability and were suitable for supercapacitor applications. Moreover, the Fe-Bi HPP material had a higher energy density value (21 Wh kg^{-1}) than the An-Bi HPP material (15 Wh kg^{-1}) [Fig. 7(c)], indicating that Fe-Bi HPP exhibited superior specific capacitance in comparison to other porous polymer electrodes [Fig. 7(d)]. Overall, these findings suggest that the Fe-Bi HPP material is a promising candidate for use in supercapacitor applications.

3.3. Iodine capture and release for Fe-Bi HPP and An-Bi HPP materials

The water contact angle (WAC) data indicates that our Fe-Bi and An-Bi HPPs demonstrate superior water compatibility and adsorption capabilities [contact angle below 40° for Fe-Bi and An-Bi HPPs, Fig. S7]. This can be attributed to the combined impact of their increased surface areas and improved hydrophilic surfaces, making them promising candidates for I_2 adsorption. We initially generated a calibration plot using an iodine/cyclohexane solution that did not contain any samples, as depicted in Fig. S8. To assess their capacity for adsorbing iodine from solution, we immersed 10 mg of each sample in an iodine/cyclohexane solution (200 mg L^{-1} , 10 mL) in a sealed glass bottle, stirred for a specified period, and then centrifuged the solution before analyzing it using UV-Visible absorption spectroscopy [Fig. 8(a) and (b)]. Our

results showed that the initial adsorption of iodine was rapid and was adsorbed faster in the initial 24 h [Fig. 8(c)], reaching equilibrium after 72 h. The maximum iodine removal efficiency values for Fe-Bi HPP and An-Bi HPP were 53.47% and 37.01%, respectively. Fe-Bi HPP exhibited higher removal efficiency than An-Bi HPP in cyclohexane solution, which could be attributed to its larger pore volume and pore size, as well as the synergistic effects of its ferrocene units, nitrogen heteroatoms, and the conjugated π -electron-rich aromatic system. To evaluate the desorption efficiency of the iodine-loaded samples (I_2 @Bi-HPPs), we measured the weight of I_2 @Bi-HPPs samples at different time intervals in the air at 130°C [Fig. 8(d)]. The iodine release efficiency was up to 85.03% and 88.56%. Our findings clearly indicate that Fe-Bi HPP has a higher adsorption capacity compared to An-Bi HPP.

Fig. 9(a) presents the adsorption isotherms of I_2 on the Fe-Bi and An-Bi HPPs. It is evident from the figure that as the initial concentration of I_2 increases, the adsorption capacity also increases. The maximum I_2 adsorption values achieved for Fe-Bi and An-Bi HPPs were 112.83 mg/g and 76.43 mg/g, respectively. The observed adsorption behavior of Fe-Bi and An-Bi HPPs can be attributed to the enhanced attraction between the I_2 ions and the adsorption sites on the adsorbent, resulting in a stronger driving force for adsorption.

The Langmuir isotherm model and the Freundlich isotherm model [shown in Fig. 9(b) and (c)] were utilized to correlate the observed I_2

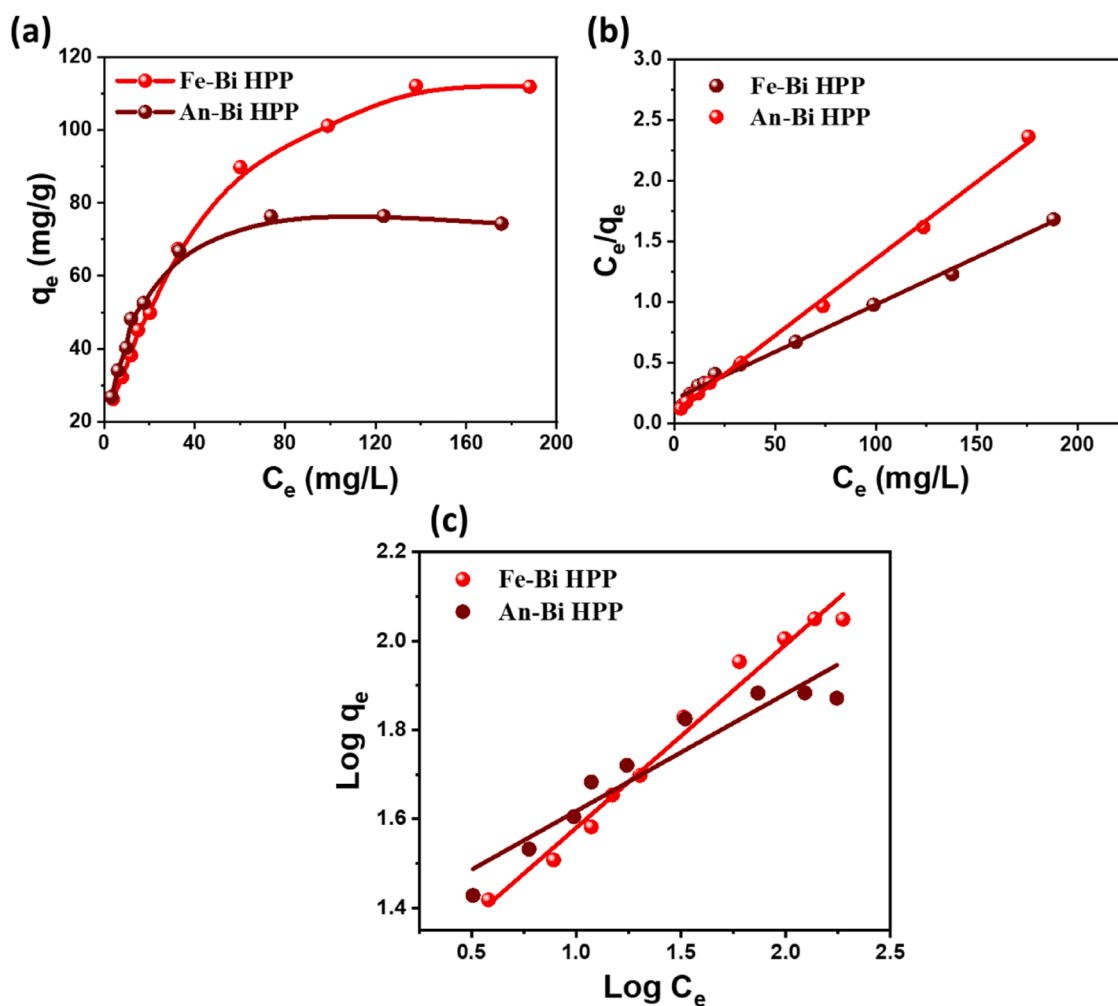


Fig. 9. (a) Adsorption isotherms of I_2 , (b) Linear fittings of the adsorption isotherm data of I_2 to Langmuir and Freundlich isotherm models using Fe-Bi and An-Bi HPPs.

Table 2
Isotherm parameters for adsorption of I_2 onto Fe-Bi and An-Bi HPPs.

Adsorbent	q_{Exp}	Langmuir			Freundlich		
		q_{max} (mg/g)	K_L (L/mg)	R^2	K_F ($mg^{1-n} L^n/g$)	$1/n$	R^2
Fe-Bi HPP	112.83	128.2	0.039	0.994	14.746	0.411	0.981
An-Bi HPP	76.43	78.92	0.142	0.998	22.599	0.263	0.908

adsorption data. These isotherm models are widely employed and offer clear equations to describe the adsorption process. Eqs. (1) and (2) depict the simplified forms of the Langmuir and Freundlich models, respectively, and the corresponding parameters are listed in Table 2.

$$\frac{C_e}{q_e} = \frac{1}{q_{max} \times K_L} + \frac{C_e}{q_{max}} \quad (1)$$

$$\log q_e = \log K_F + \frac{1}{n} \log C_e \quad (2)$$

C_e represents the concentration of I_2 in the liquid phase (measured in mg/L). q_e represents the amount of I_2 adsorbed at equilibrium (measured in mg/g), and q_{max} indicates the maximum adsorption capacity of Fe-Bi and An-Bi HPPs (measured in mg/g). The Langmuir constant (K_L , measured in L/mg) and the Freundlich constant (K_F , measured in $mg^{1-n} L^n/g$) are associated with the adsorption energy and

adsorption capacity, respectively. The Fe-Bi and An-Bi HPPs exhibited higher correlation coefficients (R^2 , 0.994 and 0.998) for the Langmuir isotherm model compared to the Freundlich isotherm (R^2 , 0.981 and 0.908). This indicates that the adsorption of I_2 by Fe-Bi and An-Bi HPPs predominantly occurs at a monolayer level, as shown in Fig. 9(b) and (c). Utilizing the Langmuir equation, the maximum adsorption capacities of I_2 on Fe-Bi and An-Bi HPPs were estimated to be 128.2 and 78.92 mg/g, respectively. These estimates closely align with the experimental measurements reported in Table 2, which are 112.83 and 76.43 mg/g, respectively.

To understand the behavior of I_2 adsorption on Fe-Bi HPP and An-Bi HPP, we conducted kinetic studies [including the pseudo-first-order, pseudo-second-order, and intraparticle diffusion models]. I_2 adsorption data fitted with the pseudo-first-order model are shown in Fig. 10(a) and (b), while the pseudo-second-order model is shown in Fig. 10(c) and (d). The intraparticle diffusion model is shown in Fig. 10(e) and (f). The kinetic characteristics of I_2 adsorption on Fe-Bi HPP and An-Bi HPP are listed in Table 3. The findings showed that for Fe-Bi HPP and An-Bi HPP, respectively, the pseudo-first-order model exhibited a coefficient of correlation (R^2) of 0.98 and 0.86. For Fe-Bi HPP and An-Bi HPP, respectively, the pseudo-second-order model showed greater coefficients of correlation of 0.99 and 0.99. These findings imply that the pseudo-second-order kinetic model more accurately captures the I_2 adsorption behavior on both materials, suggesting that chemisorption takes place during I_2 adsorption on these materials [73]. Both Fe-Bi HPP and An-Bi HPP were found to have adsorption capacities of 106.72 and

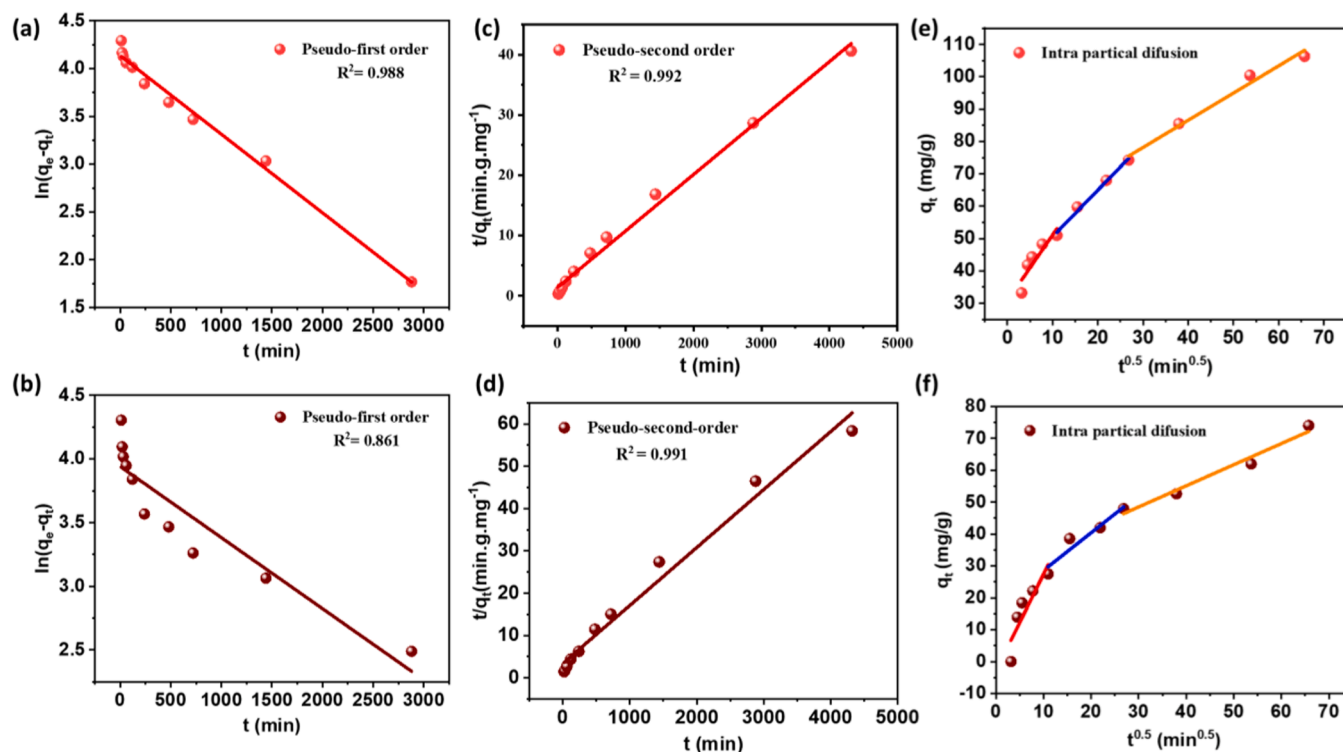


Fig. 10. The adsorption kinetic of I_2 using Fe-Bi HPP and An-Bi HPP, representing pseudo-first-order (a and b) and pseudo-second-order kinetics (c and d) for Fe-Bi HPP and An-Bi HPP, respectively, and (e and f) intraparticle diffusion for Fe-Bi HPP and An-Bi HPP, respectively. R^2 denotes the corresponding correlation coefficient value obtained via the linear fitting method.

Table 3

Kinetic parameters for adsorption of I_2 onto Fe-Bi HPP and An-Bi HPP.

Adsorbent	Pseudo-first-order			Pseudo-second-order			Intraparticle diffusion		
	q_{e1} ($mg\ g^{-1}$)	K_1 (min^{-1})	R^2	q_{e2} ($mg\ g^{-1}$)	K_2 ($g\ mg^{-1}\ min^{-1}$)	R^2	K_i	C	R^2
Fe-Bi HPP	62.51	0.0008	0.98	106.72	0.00006	0.99	1.44	36.19	0.99
An-Bi HPP	51.45	0.0005	0.86	72.94	0.00005	0.99	1.17	16.86	0.92

$72.94\ mg\ g^{-1}$, respectively. To analyze the diffusion process during I_2 adsorption, we employed the intraparticle diffusion model to fit the kinetic data. Fig. 10(e) and (f) show the relationship between q_t and $t^{0.5}$, and the adsorption curve is divided into three stages. The initial linear step represents external surface adsorption, the second step corresponds to intraparticle diffusion, and the third stage is the equilibrium stage. However, our results indicate that the intraparticle diffusion model was not applicable because the plot of q_t against $t^{0.5}$ did not yield a straight line passing through the origin. Therefore, intraparticle diffusion did not control the rate of I_2 adsorption on Fe-Bi HPP and An-Bi HPP [74]. Table 3 presents the values of K_i and C, which we calculated from the slope and intercept of the second linear stage. Figure S9 shows the schematic diagram of I_2 captures in the Fe-Bi HPP sample.

4. Conclusion

The study successfully prepared Fe-Bi HPP and An-Bi HPP materials using the Friedel-Crafts reaction and analyzed their physical properties such as specific surface area, pore size, thermal stability, and sorbent properties. Fe-Bi HPP had a thermal degradation temperature of $469\ ^\circ C$ and a char yield of 72 wt%, while An-Bi HPP had a thermal degradation temperature of $534\ ^\circ C$ and a char yield of 74 wt%. Both materials had a high specific surface area of around $850\ m^2\ g^{-1}$ and a narrow distribution of pore sizes in the micropore range, according to BET data. Electrochemical analysis showed that Fe-Bi HPP and An-Bi HPP had a

capacitance of 147 and $105\ F\ g^{-1}$ with the energy density of 21 and $15\ Wh\ Kg^{-1}$. The I_2 capture performance of Fe-Bi HPP was found to be superior to that of An-Bi HPP, which could be explained by the high surface area and the presence of the ferrocene unit in Fe-Bi HPP, resulting in a remarkable adsorption capacity of $112.84\ mg\ g^{-1}$. These results hold significant importance in devising effective techniques to minimize the possible risks linked with the waste produced by the nuclear industry.

Declaration of Competing Interest

The authors declare that they have no known competing financial interests or personal relationships that could have appeared to influence the work reported in this paper.

Acknowledgments

This study was supported financially by the Ministry of Science and Technology, Taiwan, under contracts NSTC 110-2124-M-002-013 and 111-2223-E-110-004. The authors thank National Sun Yat-sen University staff for their assistance with the TEM (ID: EM022600) experiments.

Supplementary materials

Supplementary material associated with this article can be found, in

the online version, at [doi:10.1016/j.jtice.2023.105045](https://doi.org/10.1016/j.jtice.2023.105045).

References

- Wu F, Gao J, Zhai X, Xie M, Sun Y, Kang H, Tian Q, Qiu H. Hierarchical porous carbon microrods derived from albizia flowers for high performance supercapacitors. *Carbon N Y* 2019;147:242–51. <https://doi.org/10.1016/j.carbon.2019.02.072>.
- Liu S, Kang L, Henzie J, Zhang J, Ha J, Amin MA, Hossain MSA, Jun SC, Yamauchi Y. Recent advances and perspectives of battery-type anode materials for potassium ion storage. *ACS Nano* 2021;15:18931–73. [10.1021/acsnano.1c08428](https://doi.org/10.1021/acsnano.1c08428).
- Fan B, Wang H, Li Y, Zhao Y. Composite micelle induced biomass self-assembly into N, S co-doped hierarchical porous carbon spheres with tunable properties for energy storage. *J Taiwan Inst Chem Eng* 2022;141:104606. <https://doi.org/10.1016/j.jtice.2022.104606>.
- Li C, Kong D, Wang B, Du H, Zhao J, Dong Y, Xie Y. Conjugated microporous polymer derived N, O and S co-doped sheet-like carbon materials as anode materials for high-performance lithium-ion batteries. *J Taiwan Inst Chem Eng* 2022;134:104293. <https://doi.org/10.1016/j.jtice.2022.104293>.
- Samy MM, Mohamed MG, Sharma SU, Chaganti SV, Lee JT, Kuo SW. An ultrastable tetrabenzoaphthalene-linked conjugated microporous polymer functioning as a high-performance electrode for supercapacitors. *J Taiwan Inst Chem Eng* 2023;104750. <https://doi.org/10.1016/j.jtice.2023.104750>.
- Samy MM, Mohamed MG, Kuo SW. Pyrene-functionalized tetraphenylethylene polybenzoxazine for dispersing single-walled carbon nanotubes and energy storage. *Compos Sci Technol* 2020;199:108360. <https://doi.org/10.1016/j.compscitech.2020.108360>.
- Ejaz M, Mohamed MG, Kuo SW. Solid state chemical transformation provides a fully benzoxazine-linked porous organic polymer displaying enhanced CO₂ capture and supercapacitor performance. *Polym Chem* 2023;14:2494–509. [10.1039/D3PY00158J](https://doi.org/10.1039/D3PY00158J).
- Sahoo S, Kumar R, Joanni E, Singh RK, Shim JJ. Advances in pseudocapacitive and battery-like electrode materials for high performance supercapacitors. *J Mater Chem A* 2022;10:13190–240. <https://doi.org/10.1039/D2TA02357A>.
- Chen D, Jiang K, Huang T, Shen G. Recent advances in fiber supercapacitors: materials, device configurations, and applications. *Adv Mater* 2020;32:1901806. <https://doi.org/10.1002/adma.201901806>.
- Zhao D, Wang H, Bai Y, Yang H, Song H, Li B. Preparation of advanced multi-porous carbon nanofibers for high-performance capacitive electrodes in supercapacitors. *Polymers* 2022;15:213. <https://doi.org/10.3390/polym15010213>.
- Lyu W, Yan C, Chen Z, Chen J, Zuo H, Teng L, Liu H, Wang L, Liao Y. Spirobifluorene-based conjugated microporous polymer-grafted carbon nanotubes for efficient supercapacitive energy storage. *ACS Appl Energy Mater* 2022;5:3706–14. [10.1021/acsami.2c00151](https://doi.org/10.1021/acsami.2c00151).
- Zhang Y, Gao X, Zhang Y, Gui J, Sun C, Zheng H, Guo S. High-efficiency self-charging power systems based on performance-enhanced hybrid nanogenerators and asymmetric supercapacitors for outdoor search and rescue. *Nano Energy* 2022;292:106788. <https://doi.org/10.1016/j.nanoen.2021.106893>.
- Zaw NYW, Jo S, Park J, Kitchamsetti N, Jayababu N, Kim D. Clay-assisted hierarchical growth of metal-telluride nanostructures as an anode material for hybrid supercapacitors. *Appl Clay Sci* 2022;225:106539. <https://doi.org/10.1016/j.clay.2022.106539>.
- Tomboc GM, Kim J, Wang Y, Son Y, Li J, Kim JY, Lee K. Hybrid layered double hydroxides as multifunctional nanomaterials for overall water splitting and supercapacitor applications. *J Mater Chem A* 2021;9:4528–57. <https://doi.org/10.1039/D0TA11606H>.
- Babu A, Somesh TE, Ani Dechamma CD, Hemavathi AB, Kakarla RR, Kulkarni RV, Raghav AV. Ternary structured magnesium cobalt oxide/graphene/polycarbonyl nanohybrids for high performance electrochemical supercapacitors. *Mater Sci Energy Technol* 2022;6:399–408. <https://doi.org/10.1016/j.mset.2023.04.002>.
- Septiani W, Kaneti YV, Fathoni KB, Wang J, Ide Y, Yulianto B, Nugraha B, Dipojono HK, Nanjundan AK, Golberg D, Bando Y, Yamauchi Y. Self-assembly of nickel phosphate-based nanotubes into two-dimensional crumpled sheet-like architectures for high-performance asymmetric supercapacitors. *Nano Energy* 2020;67:104270. <https://doi.org/10.1016/j.nanoen.2019.104270>.
- Mohamed MG, Mansoure TH, Takashi Y, Samy MM, Chen T, Kuo SW. Ultrastable porous organic/inorganic polymers based on polyhedral oligomeric silsesquioxane (POSS) hybrids exhibiting high performance for thermal property and energy storage. *Microporous Mesoporous Mater* 2021;328:111505. <https://doi.org/10.1016/j.micromeso.2021.111505>.
- Prabhu R, Jeevananda T, Reddy b KR, Raghu AV. Polyaniline-fly ash nanocomposites synthesized via emulsion polymerization: physicochemical, thermal and dielectric properties. *Mater Sci Energy Technol* 2021;4:107–12. <https://doi.org/10.1016/j.mset.2021.02.001>.
- Wang F, Wu X, Yuan X, Liu Z, Zhang Y, Fu L, Zhu Y, Zhou Q, Wu Y, Huang W. Latest advances in supercapacitors: from new electrode materials to novel device designs. *Chem Soc Rev* 2017;46:6816–54. <https://doi.org/10.1039/C7CS00205J>.
- Tao XY, Du J, Sun Y, Zhou SL, Xia Y, Huang H, Gan YP, Zhang WK, Li XD. Exploring the energy storage mechanism of high-performance MnO₂ electrochemical capacitor electrodes: an in situ atomic force microscopy study in aqueous electrolyte. *Adv Funct Mater* 2013;37:4745–51. <https://doi.org/10.1002/adfm.201300359>.
- Ejaz M, Samy MM, Ye Y, Kuo S-W, Mohamed MG. Design hybrid porous organic/inorganic polymers containing polyhedral oligomeric silsesquioxane/pyrene/anthracene moieties as a high-performance electrode for supercapacitor. *Int J Mol Sci* 2023;24:2501. <https://doi.org/10.3390/ijms24032501>.
- Khattak AM, Sin H, Ghazi ZA, He X, Liang B, Khan NA, Alanagh HR, Iqbal A, Li LS, Tang ZT. Controllable fabrication of redox-active conjugated microporous polymer on reduced graphene oxide for high performance faradaic energy storage. *J Mater Chem* 2018;6:18827–32. <https://doi.org/10.1039/C8TA07913G>.
- Simon P, Gogotsi Y, Dunn B. Where do batteries end and supercapacitors begin? *Science* 2014;343:1210–1. <https://doi.org/10.1126/science.1249625>.
- Yan J, Wang Q, Wei T, Fan ZJ. Recent advances in design and fabrication of electrochemical supercapacitors with high energy densities. *Adv Energy Mater* 2014;4:1300816–59. <https://doi.org/10.14478/ace.2016.1061>.
- Wang YG, Song YF, Xia YY. Electrochemical capacitors: mechanism, materials, systems, characterization and applications. *Chem Soc Rev* 2016;45:5925–50. <https://doi.org/10.1039/C5CS00580A>.
- Chang JH, Puhan A, Dong CD, Shen SY, Chandraker N, Kumar M. Synthesis of Pd-Fe₂O₃ nanoflakes nanocomposite for superior energy storage device. *J Taiwan Inst Chem Eng* 2022;140:104562. <https://doi.org/10.1016/j.jtice.2022.104562>.
- Li W, Liu J, Zhao D. Mesoporous materials for energy conversion and storage devices. *Nat Rev Mater* 2016;1:16023–40. <https://doi.org/10.1038/s41467-018-02930-9>.
- Mohamed MG, Chang SY, Ejaz M, Samy MM, Mousa AO, Kuo SW. Design and synthesis of bisulfone-linked two-dimensional conjugated microporous polymers for CO₂ adsorption and energy storage. *Molecules* 2023;28:3234. <https://doi.org/10.3390/molecules28073234>.
- Mousa AO, Lin ZI, Chuang CH, Chen CK, Kuo SW, Mohamed MG. Rational design of bifunctional microporous organic polymers containing anthracene and triphenylamine units for energy storage and biological applications. *Int J Mol Sci* 2023;24:8966. <https://doi.org/10.3390/ijms24108966>.
- Mohamed MG, EL-Mahdy AFM, Kotp MG, Kuo SW. Advances in porous organic polymers: syntheses, structures, and diverse applications. *Mater Adv* 2022;3:707–33. <https://doi.org/10.1039/D1MA00771H>.
- Samy MM, Mohamed MG, Mansoure TH, Meng TS, Khan MAR, Liaw CC, Kuo SW. Solid state chemical transformations through ring-opening polymerization of ferrocene-based conjugated microporous polymers in host-guest complexes with benzoxazine-linked cyclodextrin. *J Taiwan Inst Chem Eng* 2022;132:104110. <https://doi.org/10.1016/j.jtice.2021.10.010>.
- Mohamed MG, Samy MM, Mansoure TH, Sharma SU, Tsai MS, Chen JH, Lee JT, Yu HH, Chen T, Kuo SW. Dispersions of 1, 3, 4-oxadiazole-linked conjugated microporous polymers with carbon nanotubes as a high-performance electrode for supercapacitors. *ACS Appl Energy Mater* 2022;5:3677–88. [10.1021/acsami.2c00100](https://doi.org/10.1021/acsami.2c00100).
- Young C, Park T, Yi JW, Kim J, Hossain MSA, Kaneti YV, Yamauchi Y. Advanced functional carbons and their hybrid nanoarchitectures towards supercapacitor applications. *ChemSusChem* 2018;11:3546–58. <https://doi.org/10.1002/cssc.201801525>.
- Zheng S, Miao L, Sun T, Li L, Ma T, Bao J, Tao Z, Chen J. An extended carbonyl-rich conjugated polymer cathode for high-capacity lithium-ion batteries. *J Mater Chem A* 2021;9:2700–5. <https://doi.org/10.1039/D0TA11648C>.
- Mohamed MG, Chaganti SV, Sharma SU, Samy MM, Ejaz M, Lee JT, Zhang K, Kuo SW. Constructing conjugated microporous polymers containing the pyrene-4,5,9,10-tetraone unit for energy storage. *ACS Appl Energy Mater* 2022;5:10130–40. [10.1021/acsami.2c01842](https://doi.org/10.1021/acsami.2c01842).
- Mohamed MG, Chang WC, Kuo SW. Crown ether-and benzoxazine-linked porous organic polymers displaying enhanced metal ion and CO₂ capture through solid-state chemical transformation. *Macromolecules* 2022;55:7879–92. [10.1021/acs.macromol.2c01216](https://doi.org/10.1021/acs.macromol.2c01216).
- Mohamed MG, Chen TC, Kuo SW. Solid-state chemical transformations to enhance gas capture in benzoxazine-linked conjugated microporous polymers. *Macromolecules* 2021;54:5866–77. <https://doi.org/10.1021/acs.macromol.1c00736>.
- Mousa AO, Mohamed MG, Chuang CH, Kuo SW. Carbonized aminal-linked porous organic polymers containing pyrene and triazine units for gas uptake and energy storage. *Polymers* 2023;15:1891. <https://doi.org/10.3390/polym15081891>.
- Samy MM, Mekhemer IMA, Mohamed MG, Elsayed MH, Lin KH, Chen YK, Wu TL, Chou HH, Kuo SW. Conjugated microporous polymers incorporating Thiazol[5,4-d]thiazole moieties for sunlight-driven hydrogen production from water. *Chem Eng J* 2022;446:137158. <https://doi.org/10.1016/j.cej.2022.137158>.
- Zhang Y, Zhang B, Chen L, Wang T, Di M, Jiang F, Xu X, Qiao S. Rational design of covalent triazine frameworks based on pore size and heteroatomic toward high performance supercapacitors. *J Colloid Interface Sci* 2022;606:1534–42. <https://doi.org/10.1016/j.jcis.2021.08.087>.
- Mohamed MG, Elsayed MH, Elewa AM, EL-Mahdy AFM, Yang CH, Mohammed AAK, Chou HH, Kuo SW. Pyrene-containing conjugated organic microporous polymers for photocatalytic hydrogen evolution from water. *Catal Sci Technol* 2021;11:2229–41. <https://doi.org/10.1039/D0CY02482A>.
- Mohamed MG, Hu HY, Madhu M, Samy MM, Mekhemer IMA, Tseng WL, Chou HH, Kuo SW. Ultrastable two-dimensional fluorescent conjugated microporous polymers containing pyrene and fluorene units for metal ion sensing and energy storage. *Eur Polym J* 2023;189:111980. <https://doi.org/10.1016/j.eurpolymj.2023.111980>.
- Mohamed MG, Hu HY, Madhu M, Ejaz M, Sharma SU, Tseng WL, Samy MM, Huang CW, Lee JT, Kuo SW. Construction of ultrastable conjugated microporous polymers containing thiophene and fluorene for metal ion sensing and energy storage. *Micromachines* 2022;13:1466. <https://doi.org/10.3390/mi13091466>.

- [44] Roh DH, Shin H, Kim HT, Kwon TH. Sono-cavitation and nebulization-based synthesis of conjugated microporous polymers for energy storage applications. *ACS Appl Mater Inter* 2021;13:61598–609. <https://doi.org/10.1021/acami.1c13755>.
- [45] Loganathan NN, Perumal V, Pandian BR, Atchudan R, Edison TNJI, Ovinis M. Recent studies on polymeric materials for supercapacitor development. *J Energy Storage* 2022;49:104149. <https://doi.org/10.1016/j.est.2022.104149>.
- [46] Xiong S, Liu J, Wang Y, Wang X, Chu J, Zhang R, Gong M, Wu B. Solvothermal synthesis of triphenylamine-based covalent organic framework nanofibers with excellent cycle stability for supercapacitor electrodes. *J Appl Polym Sci* 2022;139:51510. <https://doi.org/10.1002/app.51510>.
- [47] Zheng S, Li Q, Xue H, Pang H, Xu Q. A highly alkaline-stable metal oxide@metal-organic framework composite for high-performance electrochemical energy storage. *Natl Sci* 2020;7:305–14. <https://doi.org/10.1002/app.51510>.
- [48] Shaikh NS, Ubale SB, Mane VJ, Shaikh JS, Lokhande VC, Praserttham S, Lokhande CD, Kanjanaboos P. Novel electrodes for supercapacitor: conducting polymers, metal oxides, chalcogenides, carbides, nitrides, MXenes, and their composites with graphene. *J Alloys Compd* 2022;893:161998. <https://doi.org/10.1016/j.jallcom.2021.161998>.
- [49] Mohamed MG, Sharma SU, Liu NY, Mansoure TH, Samy MM, Chaganti SV, Chang YL, Lee JT, Kuo SW. Ultrastable covalent triazine organic framework based on anthracene moiety as platform for high-performance carbon dioxide adsorption and supercapacitors. *Int J Mol Sci* 2022;23:3174. <https://doi.org/10.3390/ijms23063174>.
- [50] Mohamed MG, EL-Mahdy AFM, Takashi Y, Kuo SW. Ultrastable conductive microporous covalent triazine frameworks based on pyrene moieties provide high performance CO₂ uptake and supercapacitance. *New J Chem* 2020;44:8241–53. <https://doi.org/10.1039/D0NJ01292K>.
- [51] Mohamed MG, Zhang X, Mansoure TH, EL-Mahdy AFM, Huang CF, Danko M, Xin Z, Kuo SW. Hypercrosslinked porous organic polymers based on tetraphenylanthraquinone for CO₂ uptake and high-performance supercapacitor. *Polymer* 2020;205:122857–68. <https://doi.org/10.1016/j.polymer.2020.122857>.
- [52] Weng TH, Mohamed MG, Sharma SU, Chaganti SV, Samy MM, Lee JT, Kuo SW. Ultrastable three-dimensional triptycene-and tetraphenylethene-conjugated microporous polymers for energy storage. *ACS Appl Energy Mater* 2022;5:14239–49. <https://doi.org/10.1021/acsaem.2c02809>.
- [53] Mohamed MG, Jr Atayde EC, Matsagar BM, Na N, Yamauchi Y, Wu WCW, Kuo SW. Construction hierarchically mesoporous/microporous materials based on block copolymer and covalent organic framework. *J Taiwan Inst Chem Eng* 2020;122:180–92. <https://doi.org/10.1016/j.jtice.2020.06.013>.
- [54] Ejaz M, Mohamed MG, Chang WC, Kuo SW. Synthesis and design of hypercrosslinked porous organic frameworks containing tetraphenylpyrazine unit for high-performance supercapacitor. *J Polym Sci* 2023. <https://doi.org/10.1002/pol.20230174>.
- [55] Mohamed MG, Tsai MY, Wang CF, Huang CF, Danko M, Dai L, Chen T, Kuo SW. Multifunctional polyhedral oligomeric silsesquioxane (POSS) based hybrid porous materials for CO₂ uptake and iodine adsorption. *Polymers* 2021;13:221. <https://doi.org/10.3390/polym13020221>.
- [56] Pan L, Chen Q, Zhu JH, Yu JG, He YJ, Han BH. Hypercrosslinked porous polycarbazoles via one-step oxidative coupling reaction and Friedel–Crafts alkylation. *Polym Chem* 2015;6:2478–87. <https://doi.org/10.1039/C4PY01797H>.
- [57] Liu Y, Fan X, Jia X, Chen X, Zhang A, Zhang B, Zhang Q. Preparation of magnetic hyper-cross-linked polymers for the efficient removal of antibiotics from water. *ACS Sustain Chem Eng* 2018;6:210–22. <https://doi.org/10.1021/acssuschemeng.7b02252>.
- [58] Mohamed MG, Ahmed MMM, Du WT, Kuo SW. Meso/microporous carbons from conjugated hyper-crosslinked polymers based on tetraphenylethene for high-performance CO₂ capture and supercapacitor. *Molecules* 2021;26:738. <https://doi.org/10.3390/molecules26030738>.
- [59] Vinodh R, Gopi CVVM, Kummara VGR, Atchudanc R, Ahamad T, Sambasivam S, Yi M, Obaidat IM, Kim HJ. A review on porous carbon electrode material derived from hypercrosslinked polymers for supercapacitor applications. *J Energy Storage* 2020;32:101831. <https://doi.org/10.1016/j.est.2020.101831>.
- [60] Dong Q, Meng Z, Ho CL, Guo H, Yang W, Manners I, Xu L, Wong WY. Molecular approach to magnetic metallic nanostructures from metallopolymer precursors. *Chem Soc Rev* 2018;47:4934–53. <https://doi.org/10.1039/C7CS00599G>.
- [61] Wei Z, Wang D, Liu Y, Guo X, Zhu Y, Meng Z. Ferrocene-based hyperbranched polymers: a synthetic strategy for shape control and applications as electroactive materials and precursor-derived magnetic ceramics. *J Mater Chem C* 2020;8:10774–80. <https://doi.org/10.1039/D0TC01380C>.
- [62] Ma L, Liu Y, Liu Y, Jiang S, Li P, Hao Y, Shao P, Yin A, Feng X, Wang B. Ferrocene-linkage-facilitated charge separation in conjugated microporous polymers. *Angew Chem Int Ed* 2019;58:4221–6. <https://doi.org/10.1002/anie.201813598>.
- [63] Tan Z, Su H, Guo Y, Liu H, Liao B, Amin AM, Liu Q. Ferrocene-based conjugated microporous polymers derived from yamamoto coupling for gas storage and dye removal. *Polymers* 2020;21:2179. <https://doi.org/10.3390/polym15030719>.
- [64] Wang Y, Tao J, Xiong S, Lu P, Tang J, He J, Javaid MU, Pan C, Yu G. Ferrocene-based porous organic polymers for high-affinity iodine capture. *Chem Eng J* 2020;380:122420. <https://doi.org/10.1016/j.cej.2019.122420>.
- [65] Cao X, Wang R, Peng Q, Zhao H, Fan H, Liu H, Liu Q. Effect of pore structure on the adsorption capacities to different sizes of adsorbates by ferrocene-based conjugated microporous polymers. *Polymer* 2021;233:124192. <https://doi.org/10.1016/j.polymer.2021.124192>.
- [66] Samy MM, Mohamed MG, Kuo SW. Conjugated microporous polymers based on ferrocene units as highly efficient electrodes for energy storage. *Polymers* 2020;15:1095. <https://doi.org/10.3390/polym15051095>.
- [67] Zhang QM, Zhai TL, Wang Z, Cheng G, Ma H, Zhang QP, Zhao YH, Tan B, Zhang C. Hyperporous carbon from triptycene-based hypercrosslinked polymer for iodine capture. *Adv Mater Interfaces* 2019;6:1900249. <https://doi.org/10.1002/admi.201900249>.
- [68] Raghu AV, Gadaginamath GS, Mallikarjuna NN, Aminabhavi TM. Synthesis and characterization of novel polyureas based on benzimidazole-2-one and benzimidazole-2-thione hard segments. *J Appl Polym Sci* 2006;100:576–83. <https://doi.org/10.1002/app.23334>.
- [69] Jawalkar SS, Nataraj SK, Raghu AV, Aminabhavi TM. Molecular dynamics simulations on the blends of poly(vinyl pyrrolidone) and poly(bisphenol-A-ether sulfone). *J Appl Polym Sci* 2008;108:3572–6. <https://doi.org/10.1002/app.28005>.
- [70] Okada Y, Oguri K, Sakamoto K, Miyako Y, Hayashi T. ¹³C cross-polarization magic angle spinning NMR of ferrocene derivatives. *Magn Reson Chem* 2002;40:795–6. <https://doi.org/10.1002/mrc.1100>.
- [71] Samy MM, Sharma SU, Mohamed MG, Mohammed AAK, Chaganti SV, Lee JT, Kuo SW. Conjugated microporous polymers containing ferrocene units for high carbon dioxide uptake and energy storage. *Mater Chem Phys* 2022;278:126177. <https://doi.org/10.1016/j.matchemphys.2022.126177>.
- [72] Li Y, Wang C, Ma S, Zhang H, Ou J, Wei Y, Ye M. Fabrication of hydrazone-linked covalent organic frameworks using alkyl amine as building block for high adsorption capacity of metal ions. *ACS Appl Mater Interfaces* 2019;11:11706–14. <https://doi.org/10.1021/acami.8b18502>.
- [73] Sun H, La P, Yang R. Innovative nanoporous carbons with ultrahigh uptakes for capture and reversible storage of CO₂ and volatile iodine. *J Hazard Mater* 2017;321:210–7. <https://doi.org/10.1016/j.jhazmat.2016.09.015>.
- [74] Mahmoud MR, Rashad GM, Elewa AM, Metwally E, Saad EA. Optimization of adsorption parameters for removal of 152+154Eu(III) from aqueous solutions by using Zn-Cu-Ni ternary mixed oxide. *J Mol Liq* 2019;291:111257. <https://doi.org/10.1016/j.molliq.2019.111257>.